Award Number:  DAMD17-01-1-0216

TITLE:  Ultrasound Assisted Optical Imaging

PRINCIPAL INVESTIGATOR:     Nan Guang Chen, Ph.D.

CONTRACTING ORGANIZATION:  University of Connecticut
                           Storrs, Connecticut   06269-4133

REPORT DATE:  May 2002

TYPE OF REPORT:  Annual Summary

PREPARED FOR:  U.S. Army Medical Research and Materiel Command
               Fort Detrick, Maryland  21702-5012

DISTRIBUTION STATEMENT:  Approved for Public Release;
                         Distribution Unlimited

The views, opinions and/or findings contained in this report are
those of the author(s) and should not be construed as an official
Department of the Army position, policy or decision unless so
designated by other documentation.

20020910 061

# REPORT DOCUMENTATION PAGE

*Form Approved*
*OMB No. 074-0188*

| 1. AGENCY USE ONLY (Leave blank) | 2. REPORT DATE<br>May 2002 | 3. REPORT TYPE AND DATES COVERED<br>Annual Summary (1 May 01 - 30 Apr 02) | |
|---|---|---|---|
| **4. TITLE AND SUBTITLE**<br>Ultrasound Assisted Optical Imaging | | **5. FUNDING NUMBERS**<br>DAMD17-01-1-0216 | |
| **6. AUTHOR(S)**<br>Nan Guang Chen, Ph.D. | | | |
| **7. PERFORMING ORGANIZATION NAME(S) AND ADDRESS(ES)**<br><br>University of Connecticut<br>Storrs, Connecticut 06269-4133<br><br>E-Mail: chenng@engr.uconn.edu | | **8. PERFORMING ORGANIZATION REPORT NUMBER** | |
| **9. SPONSORING / MONITORING AGENCY NAME(S) AND ADDRESS(ES)**<br><br>U.S. Army Medical Research and Materiel Command<br>Fort Detrick, Maryland 21702-5012 | | **10. SPONSORING / MONITORING AGENCY REPORT NUMBER** | |

**11. SUPPLEMENTARY NOTES**

| 12a. DISTRIBUTION / AVAILABILITY STATEMENT<br><br>Approved for Public Release; Distribution Unlimited | 12b. DISTRIBUTION CODE |
|---|---|

**13. ABSTRACT (Maximum 200 Words)**

A DC and a frequency-domain near-infrared diffusive imaging systems have been built, tested, and calibrated. Optimal numbers of optical sources and detectors were found from computer simulations. Phantom studies have demonstrated that combined ultrasound/optical imager benefits from high spatial resolution of ultrasound and improved accuracy of reconstructed maps of optical properties. A novel image reconstruction algorithm has been proposed and implemented. It reconstructs lower orders moments of targets from limited information from a diffusive system, and is more robust than conventional iterative algorithms. Clinical study will be started soon, which will eventually test the effectiveness of this new technique for breast cancer detection.

| 14. SUBJECT TERMS<br>breast cancer, diffusive, ultrasound, near-infrared | | | 15. NUMBER OF PAGES<br>25 |
|---|---|---|---|
| | | | 16. PRICE CODE |
| 17. SECURITY CLASSIFICATION OF REPORT<br>Unclassified | 18. SECURITY CLASSIFICATION OF THIS PAGE<br>Unclassified | 19. SECURITY CLASSIFICATION OF ABSTRACT<br>Unclassified | 20. LIMITATION OF ABSTRACT<br>Unlimited |

# Table of Contents

## INTRODUCTION:

Breast cancer is the number two killer of women in United States. Mammography and ultrasound are the most common imaging modalities for breast cancer screening and diagnosis. However, X-rays see very low contrasts for human soft tissues. It's hard to differentiate tumors from other lesions such as cysts on a mammogram. Ultrasound can detect and resolve breast lesions a few millimeters in size, and can distinguish cysts from solid lesions. Nonetheless, the overlapping acoustic characteristics of benign and malignant tumors result in a low specificity of ultrasound. Currently, only 20% patients sent to biopsy have malignant tumors, and 80% patients suffer from unnecessary biopsy. The purpose of this research is to develop a combined ultrasound and near-infrared diffusive imager that can significantly improve the specificity for breast cancer detection and reduce the unnecessary biopsy rate. Functional imaging with near-infrared light is based on diffusive propagation of photons inside turbid media such as breast tissues. It has been reported that this new imaging modality has the potential to differentiate breast tumors from normal surrounding tissues through determination of optical properties at different wavelengths. Some physiological parameters, such as blood volume, hemoglobin oxygenation level, and water concentrations can be retrieved from optical measurements. However, the diffusive optical imaging method alone cannot readily be applied to clinical diagnosis because of its low spatial resolution and some difficulties in image reconstruction. Combination of ultrasound and near-infrared diffusive imaging benefits from high spatial resolution of ultrasound and functional contrasts from optical imaging. In addition, a priori morphological information about embedded lesions from ultrasound can help improve the accuracy of optical image reconstruction. In this research, we have investigated the probe design involving arrangement of ultrasound transducer and optical light guides, and optimization of source and detector numbers. A frequency-domain and a DC diffusive optical imaging systems have been built and calibrated. Phantom studies have been carried out, and new image reconstruction algorithms have been proposed and validated. Our research results have been reported in a series of journal papers and conference presentations. In the next step, we will use our combined imager in Hartford Hospital and UConn Health Center and gather clinical experimental results. We will look into further problems emerging from clinical situations and improve our imaging systems as well as image reconstruction algorithms. Correlations between combined ultrasound/optical images with biopsy results will be established after clinical studies.

## BODY:

The optical sources and detector numbers and their deployment on a probe are among critical issues concerning diffusive optical imaging. Because of the diffusive nature of near-infrared light migrating through human soft tissues, more light sources and sensors do not necessarily provide more independent information. On the other hand, the system cost and data acquisition time increase with the numbers of sources and detectors. We

conducted computer simulation to find the optimal number and the best arrangement. In our simulation, a total of 364 optical source-detector pairs were deployed uniformly over a 9 cm x 9 cm probe area initially. Then the total pairs were reduced gradually to 60 in experimental and simulation studies. For each source-detector configuration, three-dimensional images of a 1-cm-diameter absorber of different contrasts were reconstructed from the measurements made with a frequency-domain system. The results have shown that more than 160 source-detector pairs are needed to reconstruct the absorption coefficient to within 60% of the true value and appropriate spatial and contrast resolution. However, the error in target depth was more than 1 cm in all source-detector configurations. With the a priori target depth information provided by ultrasound, the accuracy of the reconstructed absorption coefficient was improved by 15% and 30% on average. The speed of reconstruction was improved by ten times on average. As the ultrasound transducer needs to be placed in the middle of a probe, we have experimentally evaluated the effects of missing optical sensors in the middle of the combined probe upon the accuracy of the reconstructed optical absorption coefficient, and assessed the improvements of reconstructed absorption coefficient with the guidance of the co-registered ultrasound. The results have shown that when the central ultrasound array area is in the neighborhood of 2 x 2 cm$^2$, which corresponds to the size of most commercial ultrasound transducers, the optical image quality is not affected. The results also shown that the iterative inversion algorithm converges very fast with the guidance of *a priori* target spatial distributions.

We have constructed a near-infrared frequency-domain imaging system. This system features multiple transmission, parallel reception, and dual wavelengths. On the transmission part, 12 pairs of dual wavelength (780nm and 830nm) laser diodes are used as light sources, and their outputs are amplitude modulated at 140.000 MHz. To reduce noise and interference, an individual driving circuit is built for each diode. As laser diode works in series, a control board that interprets instructions from a PC is used to coordinate operations of associated components. When one transmission channel is selected, it turns on corresponding driving circuit so that a DC driving current can be set up for the diode. At the same time, a selected signal is sent to a RF switching unit, which distributes RF signal to the right channel to modulate the optical output. On the reception part, 8 Photo Multiplier Tubes (PMTs) are employed to detect diffusely reflected light from turbid media. Each PMT is housed in a sealed aluminum box, shielding both environment lights and electromagnetic fields, while an optical fiber (3 mm in diameter) couples NIR light from the detection point to the reception window of the PMT. The electrical signal converted from optical input is generally very weak and rather high in frequency, so high gain amplification and frequency transform are necessary before it can be sampled by an A/D board inside the PC. We have built 8 parallel heterodyne amplification channels so as to measure the response of all detectors simultaneously, thus to reduce the data acquisition time. Each amplification channel consists of a RF amplifier (40dB), a mixer where RF signal (140.000 MHz) is mixed with a local oscillator (140.020 MHz) and, a band pass filter centered at 20 KHz, and a low frequency amplifier of 30dB. The heterodyned two-stage amplification scheme helps suppress wide band noises efficiently. Eight detection signals are sampled, converted, and acquired into the PC simultaneously, in which Hilbert transform is used to compute the amplitude and

phase of each channel. The entire data acquisition is less than 15 seconds, which is fast enough to acquire data from patients.

A DC system has also been built for comparing its performance with that of a frequency-domain system. The DC system has 6 pairs of dual wavelength sources (780 nm and 830 nm). There are 12 detection light guides that collect photons from 12 positions and are coupled to a PMT through a mechanical multiplexer. The multiplexer is implemented by a rotating plate driven by a stepper motor. Although the total data acquisition speed is slow (about 1 minute for a complete scan), the DC system is far more compact than the frequency domain system and costs much less. We have tested and calibrated both systems with phantoms.

To avoid the problems related to iterative image reconstruction algorithms, we proposed a novel non-iterative method using minimal *a priori* co-registered ultrasound information. Small absorbing targets embedded in a homogeneous background are described approximately in terms of their monopole, dipole, and quadrupole moments. With an approximate estimation of center locations of these absorbers from ultrasound images, we show in simulations that the reconstruction accuracy in absorption coefficient exceeds 80% if the noise level is less than 0.2%. We also demonstrate experimentally that the accuracy can be improved by using additional ultrasound volume information even for a noise level as high as 1.5%. In the moment-based method, we assume that the lesions are isolated and are imbedded in a homogeneous background. This assumption is quite true for more homogeneous fatty breasts and may not hold for dense breasts that consist of both glandular tissue and fat. In the latter case, we could segment ultrasound images, identify tissue types and estimate background optical properties of different tissues in the reconstruction as well. Both acoustic and optical contrasts exist in tumors but the sensitivities of these two modalities may be different. Therefore, correlation between acoustic and optical heterogeneities remains unknown at the current stage and will be answered by our future clinical studies.

**KEY RESEARCH ACCOMPLISHMENTS:**
- Built a frequency-domain near-infrared diffusive imaging system, which has 12 pairs of dual-wavelength sources and 8 detectors.
- Built a DC near-infrared diffusive imaging system, which has 6 pairs of dual-wavelength sources and 12 detector positions coupled to 1 PMT by a mechanical multiplexer.
- Tested and calibrated both the frequency-domain and DC systems with phantoms.
- Found the optimal numbers of sources and detectors from computer simulations.
- Conducted phantom studies with combined ultrasound/optical imager. Investigated the effect of central ultrasound transducer on the optical image quality. Demonstrated that a priori target information from ultrasound significantly improved the accuracy of reconstructed values of optical properties.
- Propose a novel diffusive image reconstruction method based on lower order moments of embedded targets inside homogeneous turbid media.

**REPORTABLE OUTCOMES:**

Journal papers:
[1] N. G. Chen and Q. Zhu, "Characterization of small absorbers inside turbid media," Optics Letters , Vol 27, No. 4, pp 252-254 (2002).
[2] Q. Zhu, N. G. Chen, , P. Y. Guo, , S. K. Yan, and D. Q. Piao, , "Near infrared diffusive light imaging with ultrasound localization," OSA Optics and Photonics News, Optics in 2001, 12:31, December 2001
[3] N. G. Chen, P. Guo, S. Yan, D. Piao, and Q. Zhu, "Simultaneous near infrared diffusive light and ultrasound imaging," Applied Optics, vol. 40, No. 34, pp 6367-6280, 2001.
[4] Q. Zhu, N. G. Chen, X. H. Ding, D. Piao, and P. Guo, "Design of near infrared imaging probe with the assistance of ultrasound localization," Applied Optics, vol. 40, No. 19, pp 3288-3303, 2001.

Presentations:
[1] N. G. Chen, and Q. Zhu, "Nonlinear correction method for characterizing small absorbers in turbid media," OSA Biomedical Topical Meeting, Miami Beach, March 2002.
[2] Minming Huang, Tuqiang Xie, Nan Guang Chen, and Quing Zhu, "NIR imaging reconstruction with ultrasound guidance: Finite element method," OSA Biomedical Topical Meeting, Miami Beach, March 2002.

Funding applied for:
[1] Donaghue Medical Research Foundation: Co-PI, "3D simultaneous Ultrasound and Near Infrared Diffusive Imaging for Breast Cancer Detection;"
[2] NIH: Co-PI, "Near Infrared Diffused Light Imaging with Ultrasound Guidance."

**CONCLUSIONS:**

I have successfully finished the Task 1 specified in the statement of work of my proposal. A DC and a frequency-domain near-infrared diffusive imaging systems have been built, tested, and calibrated. Phantom studies have demonstrated the advantages of the combined ultrasound/optical imager. A novel image reconstruction algorithm has been proposed and implemented. I am preparing for the clinical study that will eventually test the effectiveness of this new technique for breast cancer detection.

**REFERENCE:**

[1] N. G. Chen and Q. Zhu, "Characterization of small absorbers inside turbid media," Optics Letters , Vol 27, No. 4, pp 252-254 (2002).
[2] Q. Zhu, N. G. Chen, , P. Y. Guo, , S. K. Yan, and D. Q. Piao, , "Near infrared diffusive light imaging with ultrasound localization," OSA Optics and Photonics News, Optics in 2001, 12:31, December 2001
[3] N. G. Chen, P. Guo, S. Yan, D. Piao, and Q. Zhu, "Simultaneous near infrared diffusive light and ultrasound imaging," Applied Optics, vol. 40, No. 34, pp 6367-6280, 2001.

[4] Q. Zhu, N. G. Chen, X. H. Ding, D. Piao, and P. Guo, "Design of near infrared imaging probe with the assistance of ultrasound localization," Applied Optics, vol. 40, No. 19, pp 3288-3303, 2001.

[5] N. G. Chen, and Q. Zhu, "Nonlinear correction method for characterizing small absorbers in turbid media," OSA Biomedical Topical Meeting, Miami Beach, March 2002.

[6] Minming Huang, Tuqiang Xie, Nan Guang Chen, and Quing Zhu, "NIR imaging reconstruction with ultrasound guidance: Finite element method," OSA Biomedical Topical Meeting, Miami Beach, March 2002.

**APPENDICES:**

Copies of recent journal papers:

[1] N. G. Chen and Q. Zhu, "Characterization of small absorbers inside turbid media," Optics Letters , Vol 27, No. 4, pp 252-254 (2002).

[2] N. G. Chen, P. Guo, S. Yan, D. Piao, and Q. Zhu, "Simultaneous near infrared diffusive light and ultrasound imaging," Applied Optics, vol. 40, No. 34, pp 6367-6280, 2001.

# Characterization of small absorbers inside turbid media

Nan Guang Chen and Quing Zhu

*Department of Electrical & Computer Engineering, University of Connecticut, Storrs, Connecticut 06269*

We propose a novel noniterative near-infrared diffusive image reconstruction method that uses minimal *a priori* co-registered ultrasound information. Small absorbing targets embedded in a homogeneous background are described approximately in terms of their monopole, dipole, and quadrupole moments. With an approximate estimation of the center locations of these absorbers from ultrasound images, we show in simulations that the reconstruction accuracy of the absorption coefficient exceeds 80% if the noise level is less than 0.2%. We also demonstrate experimentally that the accuracy can be improved by use of additional ultrasound volume information even for a noise level as high as 1.5%.  © 2002 Optical Society of America

*OCIS codes:* 100.3190, 170.3010, 170.3880, 290.1990.

Functional imaging with near-infrared (NIR) light has found potential applications in many areas, such as breast and brain lesion detection and diagnosis.[1,2] Recently, a combination of NIR imaging with other imaging modalities, such as ultrasound or magnetic resonance imaging, has shown promising results[3-5] in providing complementary contrasts and overcoming NIR reconstruction problems related to intensive light scattering.

In this Letter we introduce a novel reconstruction algorithm for NIR diffusive imaging that uses approximate target center locations estimated from co-registered ultrasound. Our new method is based on estimation of major characteristics of isolated small absorbers. These characteristics are monopole, dipole, and quadrupole moments. Higher-order moments have negligible effects in characterizing the absorbers and are ignored. It is shown in this Letter that measurements of diffusive photon density waves cannot readily achieve a signal-to-noise ratio that is good enough for reconstructing the detailed shape information of targets. However, the quadrupole moment can provide an approximate extension of the target, which is necessary for distributing the integral absorption (the monopole) to an appropriate target region. In situations in which the measurement system suffers from unexpected noise, accurate estimation of the quadrupole moment might not be possible. The target volume estimated from co-registered ultrasound images can be used for distributing the integral absorption inside the target volume. We have conducted a series of simulations at different noise levels to evaluate the performance of this new method. We have also conducted experiments using our combined NIR–ultrasound imager[5] to test the algorithm.

If it is assumed that there are only a few small inhomogeneous targets embedded in a homogeneous background, the distribution of the absorption coefficient can be expressed as

$$\mu_a(\mathbf{r}) = \mu_a{}^0 + \Delta\mu_a(\mathbf{r}).  \tag{1}$$

The background absorption coefficient, $\mu_a{}^0$, can be as small as 0.02 cm$^{-1}$ for normal breast tissues, whereas $\Delta\mu_a$ can be well beyond 0.1 cm$^{-1}$ for tumors because of the blood. In the Born approximation, the photon

density wave is decomposed into an incident wave and a scattering wave:

$$\Phi(\omega, \mathbf{r}) = \Phi_{\text{inc}}(\omega, \mathbf{r}) + \Phi_{\text{sct}}(\omega, \mathbf{r}).  \tag{2}$$

The incident wave is the solution of a homogeneous diffusion equation, and the scattering wave can be given approximately by the linear perturbation theory:

$$\Phi_{\text{sct}}(\omega, \mathbf{r}) \approx -\int_V \frac{\Delta\mu_a(\mathbf{r}')}{D}\, \Phi_{\text{inc}}(\omega, \mathbf{r}')G(\mathbf{r}, \mathbf{r}')d^3\mathbf{r}'.  \tag{3}$$

In this equation, $G(\mathbf{r}, \mathbf{r}')$ is the Green's function, and $D = 1/3\mu_s'$ is inversely proportional to the reduced scattering coefficient, $\mu_s'$. In the context of early stage breast cancer detection, we can further assume that those heterogeneities are confined to a few isolated regions. Then, the scattering wave can be expanded around each of $N$ target centers as

$$\Phi_{\text{sct}}(\omega, \mathbf{r}) = -\frac{1}{D} \sum_{\nu=1}^{N} [M^\nu W(\mathbf{r}_0{}^\nu) + \mathbf{D}^\nu \cdot \nabla W(\mathbf{r}_0{}^\nu)$$
$$+ \mathbf{Q}^\nu \cdot \nabla\nabla W(\mathbf{r}_0{}^\nu)/2 + O(a^3)].  \tag{4}$$

Here $\mathbf{r}_0{}^\nu$ is the center of the $\nu$th target, and $W(\mathbf{r}_0{}^\nu) = \Phi_{\text{inc}}(\omega, \mathbf{r}_0{}^\nu)G(\mathbf{r}, \mathbf{r}_0{}^\nu)$ is the weight function. For the $\nu$th target, $M^\nu$, $\mathbf{D}^\nu$, and $\mathbf{Q}^\nu$ are its monopole, dipole, and quadrupole moments, respectively. Terms beyond the second order of target dimension $a$ have negligible effects in characterizing the absorbers and are neglected in our model. For the $\nu$th target, its monopole, dipole, and quadrupole moments are scalar, vector, and second-order tensor, respectively, and they are given as

$$M^\nu = \int_{V_\nu} \Delta\mu_a(\mathbf{r}')d^3\mathbf{r}', \qquad \mathbf{D}^\nu = \int_{V_\nu} \Delta\mu_a(\mathbf{r}')\mathbf{r}'d^3\mathbf{r}',$$

$$\mathbf{Q}^\nu = \int_{V_\nu} \Delta\mu_a(\mathbf{r}')\mathbf{r}'\mathbf{r}'d^3\mathbf{r}'.  \tag{5}$$

The integrations are over a small isolated region $V_\nu$.

A multiple-source, multiple-detector configuration is typical for frequency-domain diffusive imaging systems. We are using 12 sources (780 nm) that are amplitude modulated at 140 MHz and eight detectors

in our simulations as well as in the experiments. These sources and detectors are deployed on an absorbing plane, which simplifies boundary conditions. The reflection mode with a semi-infinite geometry is used for both simulation and experiment. The measured scattering wave is related to the target moments by the following equation:

$$[\hat{\phi}_1 \cdots \hat{\phi}_m]^T \approx \Omega[M^1 \quad D^1 \quad Q^1 \quad \cdots \quad Q^N]^T. \quad (6)$$

An element of $\Omega$ is either the weight function for one target or its derivatives up to the second order.

The inverse problem is to retrieve the characteristics of those embedded absorbers from measured photon density waves on the surface. Based on our simplified forward model, it is necessary to have certain information about absorbers, such as the number of targets and their center positions, in advance. The ultrasound system of our combined imager can provide such information. Once the initial center locations have been specified, the weight function, together with its first and second derivatives, can be calculated immediately. Since the inverse problem has only a few unknowns, reconstruction of target moments is overdetermined and least-squares solutions can be adopted. For each target, the monopole moment represents the integral absorption, the dipole moments result in correction of the center position, and the quadrupole moments lead to estimation of the target volume, in which the integral absorption can be redistributed. The target volume is estimated by simple matching of the quadrupole moments with those of an ellipsoid, which has the freedom to rotate about the center in any direction to any angle.

Figure 1 shows a schematic of the combined probe for experiments, which is a circular plate made of rigid absorbing material. One or two cuboid absorbers were placed 2.5 cm deep in a homogeneous medium. For phantom experiments, raw data were acquired with our combined imaging system. The ultrasound array was translated in the $x$ direction to yield target volume estimates. We used 0.6% Intralipid as a homogeneous background, which yielded a reduced scattering coefficient of 6 cm$^{-1}$ and an absorption coefficient of 0.015 cm$^{-1}$. The embedded targets were as scattering as the background but were more absorbing. For simulations, the simulated measurement data were the sum of forward model prediction and random noises ranging from 0.1% to 1% (with respect to the amplitudes of the incident waves). The optical properties of homogeneous media and targets are similar to those used in phantom experiments.

Shown in Fig. 2 are simulation results for a single target. The target was a cuboid of (1.2, 0.8, 1) cm in the $x$, $y$, and $z$ directions, respectively, and was centered at (0.2, 0, 2.5) cm. The volume of the target was 0.96 cm$^3$. The absorption coefficient above the background was 0.25 cm$^{-1}$. Here we provide the results for one dipole moment ($D_x$) and one quadruple moment ($Q_{xx}$), but similar results were obtained for other components. The initial target position that was input into the reconstruction algorithm was (0,

0, 2.5) cm, which deviated slightly from the true position. This initial location error resulted in a negligible effect on the reconstructed monopole values, as shown in Fig. 2(a). The offset of center position can be corrected by the estimated dipole moment, $D_x$ [see Fig. 2(c)], which is slightly lower than the true value. However, the inaccuracy of the initial center position obviously affects the reconstructed quadrupole moment. The circles in Fig. 2(e) represent values greater than the true values. After we correct the center position according to the estimated dipole moments, the reconstructed values of $Q_{xx}$, plotted as asterisks in the same figure, are much closer to the true values. Although the mean values of reconstructed moments are essentially independent of noise
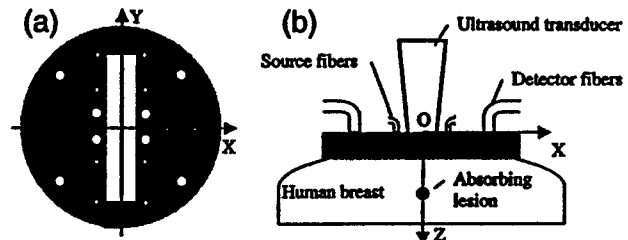


Fig. 1. (a) Bottom view of the combined probe. The central rectangular slot gives the ultrasound array access to tissues underneath the probe. The circular holes are used to hold optical fibers. The small holes are for light sources, and the larger ones are for detectors. The diameter of the probe is 10 cm. (b) Side view of the probe.
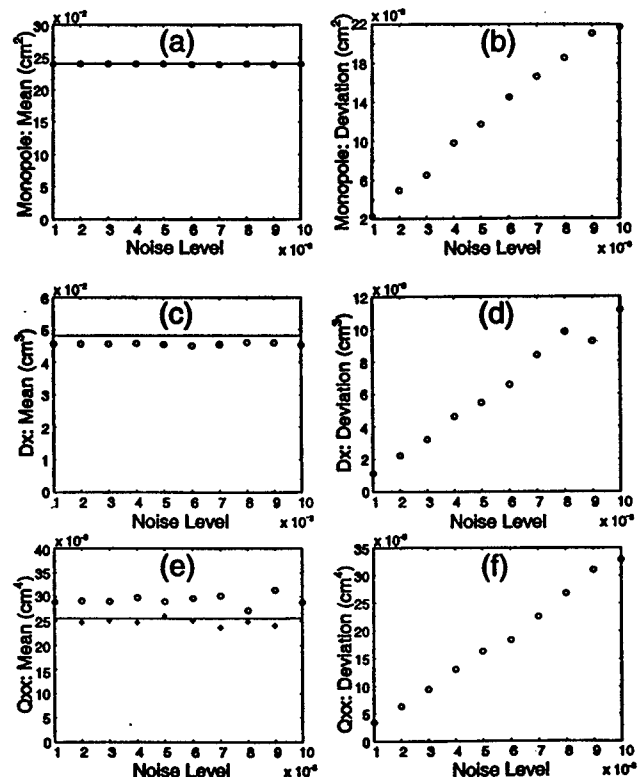


Fig. 2. Simulation results for a single target. (a), (c), and (e) mean values of monopole, dipole, and quadrupole moments, respectively. (b), (d), and (f) standard deviations of the corresponding quantities. The solid lines in (a), (c), and (e) are true values.

**Table 1.  Reconstructed Absorption Coefficients from Phantom Experiments**[a]

| Value (cm⁻¹) | Combination 1 | | Combination 2 | |
| --- | --- | --- | --- | --- |
| | Target 1 | Target 2 | Target 1 | Target 2 |
| True | 0.065 | 0.065 | 0.102 | 0.065 |
| Reconstructed | $0.064 \pm 0.028$ | $0.064 \pm 0.027$ | $0.106 \pm 0.026$ | $0.064 \pm 0.017$ |

[a]The average values and standard deviations are estimated from six sets of experimental data.

level, the standard deviations of all moments increase linearly with increasing noise level. Higher-order moments suffer more from noise, as expected intuitively. For the quadrupole moments, as small as a 0.2% noise level could lead to a relative error of ~20%. This is the main reason that we did not attempt to reconstruct moments beyond the second order.

To test the capability of our algorithm to characterize multiple targets, we performed simulations with two absorbers of different absorption coefficients. The absorbers were the same size as the single target. One absorber was located at $(-1.2, 0, 2.5)$ cm, with an absorption coefficient $0.25$ cm⁻¹ beyond the background. The other absorber was located at $(1.2, 0, 2.5)$ cm, with an absorption coefficient $0.1$ cm⁻¹ beyond the background. The main effect of adding one target was that the relative error in the reconstructed monopole moments increased to ~2.5 times. Less of an effect on the dipole moments was observed, although an even more trivial difference for the quadrupole could be seen. It was also found that the noise-induced deviation was independent of target optical properties.

Our current NIR imaging system has a noise level near 1.5%. According to the simulation results, the system cannot readily retrieve the accurate quadrupole moments from measured photon density waves. Thus we have to use the volume information obtained from co-registered ultrasound images in target characterization. We used two geometrically identical targets that were approximately 1-cm³ cubes. They were gel phantoms made from 0.6% Intralipid solution, ink, and ultrasound scatterers. The boundaries of these targets can clearly be seen in ultrasound images, and target centers and volumes can be estimated accurately. For example, a 1.07-cm³ target was measured as 1.05 cm³ by ultrasound. For co-registered NIR imaging, two different combinations of targets were adopted. The first was a pair of equally absorbing cubes with an absorption coefficient of 0.065 cm⁻¹. The second was a pair of absorbing cubes with absorption coefficients of 0.065 and 0.1 cm⁻¹, respectively. We simply distribute the estimated monopole evenly over the target volume. So the reconstructed absorption coefficient was an average value within each target. The true and the reconstructed values are compared in Table 1. The mean values and standard deviations were based on six sets of measurements.

Since target monopole moments can be estimated with sufficient accuracy, the reconstructed absorption coefficient depends more on the estimation of target volume, which can be obtained from the reconstructed quadrupole moment or co-registered ultrasound images. It is possible that the extent of the optical volume of a lesion is larger than the volume esti-

mated from the acoustic images. This is one of our motivations for estimating the optical volume from the quadrupole moments. Further improvements are needed for an accurate estimate of quadrupole moments. In the moment-based method we assume that the lesions are isolated and are embedded in a homogeneous background. This assumption is quite true for more-homogeneous fatty breasts and may not hold for dense breasts that consist of both glandular tissue and fat. In the latter case, we could segment ultrasound images, identify tissue types, and estimate background optical properties of different tissues in the reconstruction as well. Both acoustic and optical contrasts exist in tumors but the sensitivities of these two modalities may be different. Therefore, the correlation between acoustic and optical heterogeneities remains unknown at the current stage and will be determined in our future clinical studies.

In comparison with current sophisticated NIR image reconstruction algorithms, our method is very simple in terms of computation. Once an ultrasound image has been taken and targets have been identified, it is possible tô monitor the local change of absorption continuously and in real time. Averaging over a large number of samples will help suppress the effect of random noise.

In this Letter an algorithm for characterizing absorbers has been demonstrated. Theoretically, a similar algorithm is possible for characterizing scattering targets as well. However, since the weights of monopole, dipole, and quadrupole moments of scattering targets are related to spatial derivatives, which are two order higher than those of absorbers, the quadrupole moments will be even harder to reconstruct.

**References**

1. B. Tromberg, N. Shah, R. Lanning, A. Cerussi, J. Espinoza, T. Pham, L. Svaasand, and J. Butler, Neoplasia **2**, 26 (2000).
2. R. M. Danen, Y. Wang, X. D. Li, W. S. Thayer, and A. G. Yodh, Photochem Photobiol. **67**, 33 (1998).
3. B. Pogue and K. Paulsen, Opt. Lett. **23**, 1716 (1998).
4. Q. Zhu, N. G. Chen, D. Q. Piao, P. Y. Guo, and X. H. Ding, Appl. Opt. **40**, 3288 (2001).
5. N. G. Chen, P. Y. Guo, S. K. Yan, D. Q. Piao, and Q. Zhu, Appl. Opt. **40**, 6367 (2001).

# Simultaneous near-infrared diffusive light and ultrasound imaging

Nan Guang Chen, Puyun Guo, Shikui Yan, Daqing Piao, and Quing Zhu

We have constructed a near-real-time combined imager suitable for simultaneous ultrasound and near-infrared diffusive light imaging and coregistration. The imager consists of a combined hand-held probe and the associated electronics for data acquisition. A two-dimensional ultrasound array is deployed at the center of the combined probe, and 12 dual-wavelength laser source fibers (780 and 830 nm) and 8 optical detector fibers are deployed at the periphery. We have experimentally evaluated the effects of missing optical sources in the middle of the combined probe on the accuracy of the reconstructed optical absorption coefficient and assessed the improvements of a reconstructed absorption coefficient with the guidance of the coregistered ultrasound. The results have shown that, when the central ultrasound array area is in the neighborhood of 2 cm × 2 cm, which corresponds to the size of most commercial ultrasound transducers, the optical imaging is not affected. The results have also shown that the iterative inversion algorithm converges quickly with the guidance of a priori three-dimensional target distribution, and only one iteration is needed to reconstruct an accurate optical absorption coefficient. © 2001 Optical Society of America

OCIS codes:  170.0170, 170.3010, 170.5270, 170.7170, 170.3830.

## 1. Introduction

Ultrasound is used extensively for differentiation of cysts from solid lesions in breast examinations, and it is routinely used in conjunction with mammography. Ultrasound can detect breast lesions a few millimeters in size.[1] However, its specificity in breast cancer diagnosis is not considered to be high enough as a result of overlapping characteristics of benign and malignant lesions.[2,3] Optical imaging based on diffusive near-infrared (NIR) light has the great potential to differentiate tumors from normal breast tissues through determination of tissue parameters, such as blood volume, blood $O_2$ saturation, tissue light scattering, water concentration, and the concentration and lifetime of exogenous contrast agents.[4-12] As a potential diagnostic tool, however, NIR diffusive light imaging suffers from low spatial resolution and lesion location uncertainties because of intense light scattering in tissue.

Most NIR imaging reconstruction algorithms are based on tomographic inversion techniques.[13-20] Reconstruction of tissue optical properties in general is underdetermined and ill-posed because the total number of unknown optical properties always exceeds the number of measurements, and the perturbations produced by the heterogeneities are much smaller than the background signals. In addition, the inversion reconstruction algorithms are sensitive to measurement noise and model errors.

Our group and others have introduced a novel hybrid imaging method that combines the complementary features of ultrasound and NIR diffusive light imaging.[21-25] The hybrid imaging obtains coregistered ultrasound and NIR diffusive light images through simultaneous deployment of an ultrasound array and NIR source–detector fibers on the same probe.[21,22,24] Coregistration permits joint evaluation of acoustic and optical properties of breast lesions and enables use of lesion morphology provided by high-resolution ultrasound to improve the lesion optical property estimate. With the a priori knowledge of lesion location and shape provided by coregistered ultrasound, NIR imaging reconstruction can be localized within specified three-dimensional (3-D) regions. As a result, the reconstruction is overdetermined because the total number of unknown optical properties is reduced significantly. In addition, the reconstruction is less sensitive to noise because the

convergence can be achieved with a small number of iterations.

The clinical use of the combined diagnosis relies on the coregistration of both ultrasound and NIR sensors at the probe level. Conventional ultrasound pulse-echo imaging requires that an imaging transducer be located on top of the target, whereas NIR diffusive light imaging is feasible when the optical source and detector fibers are distributed at the periphery of the ultrasound transducer. However, the effects of missing optical sources in the middle of the combined probe on the accuracy of the reconstructed optical properties have to be evaluated. In addition, the improvements of reconstructed optical properties with the guidance of the coregistered ultrasound need to be quantitatively assessed. Furthermore, real-time data acquisition is necessary to avoid errors in coregistration caused by patient motion during the clinical experiments. In this paper we report our experimental results on the optimal probe configuration, and we quantify the improvements on reconstructed optical properties using a combined probe. We also demonstrate simultaneous combined imaging with a near-real-time imager.

## 2. Near-Infrared Diffusive Wave Imaging

We used the Born approximation to relate the scattered field $U_{sc}'(r, \omega)$ measured at the probe surface to absorption variations in each volume element within the sample. In the Born approximation, the scattered wave originated from a source at $r_{si}$, and measured at $r_{di}$ it can be related to the medium absorption heterogeneity $\Delta\mu_a(r_{vj})$ at $r_{vj}$ by

$$[U_{sd}]_{M \times 1} = [W]_{M \times N}\{\Delta\mu_a\}_{N \times 1} \qquad (1)$$

where $M$ is the total number of source–detector pairs, $N$ is the total number of imaging voxels, and $W_{ij} = G(r_{vj}, r_{di}, \omega)U_{inc}(r_{vj}, r_{si}, \omega)v\Delta r_v^3/\bar{D}$ is the weight matrix given in Ref. 19. $G(r_{vj}, r_{di}, \omega)$ and $U_{inc}(r_{vj}, r_{si}, \omega)$ are a Green's function and incident wave, respectively. $\omega$ is the modulation frequency and $\bar{D}$ is the average or background diffusion coefficient, which is the average value over the background or whole tissue.

With M measurements obtained from all possible source–detector pairs in the planar array, we can solve $N$ unknowns of $\mu_a$ by inverting the above matrix equation. In general, the perturbation Eq. (1) is underdetermined $(M < N)$ and ill-posed.

NIR imaging by itself generally has poor depth discrimination. However, ultrasound is excellent in providing accurate target depth. Once the target depth is available from coregistered ultrasound, we can set $\Delta\mu_a$ of a nontarget depth equal to zero. This implies that all the measured perturbations originate from the particular depth that contains the target. Because the number of unknowns is reduced significantly, the reconstruction converges very fast. In Ref. 23 we reported that, with a priori target depth provided by ultrasound, the accuracy of the reconstructed $\mu_a$ has been improved by 15–30% on aver-

age, and the speed of reconstruction has been improved by an order of magnitude. In this paper we furthermore demonstrate that, with the 3-D target distribution provided by coregistered ultrasound, the accuracy of reconstructed $\mu_a$ and the reconstruction speed can be further improved.

To solve the unknown optical properties of Eq. (1), we used the total least-squares (TLS) method[26,27] to iteratively invert Eq. (1). The TLS method performs better than other least-squares when the measurement data are subject to noise and the linear operator $W$ contains errors. We found that the TLS method provides more accurate reconstructed optical properties than other least-squares methods, and we adopted TLS in solving inverse problems. It has been shown in Ref. 28 that the TLS minimization is equivalent to the following minimization problem:

$$\min \frac{\|U_{sd} - WX\|^2}{\|X\|^2 + 1}, \qquad (2)$$

where $X$ represents unknown optical properties. The conjugate gradient technique was employed to iteratively solve Eq. (2).

## 3. Methods

### A. Combined Probe and Imaging Geometry

There are four basic requirements to guide the design of the combined probe. First, reflection geometry is preferred because a conventional ultrasound scan is performed with this geometry. Second, an ultrasound array needs to occupy the center of the combined probe for coherent imaging. Third, NIR sources and detectors have to be distributed at the periphery. Because photon propagation distribution exhibits a banana shape, imaging of the tissue volume underneath the probe is feasible even through there are no sources and detectors deployed in the central portion of the probe. Fourth, the minimum source–detector separation should be larger than 1 cm for the diffusion approximation to be valid, and the maximum separation should be ~8–9 cm to effectively probe depths of 3–4 cm.

On the basis of these requirements we deployed 12 dual-wavelength optical source fibers and 8 detector fibers over a 9 cm × 9 cm probe area (see Fig. 1). The minimum and maximum source–detector separations in the configuration are 1.4 and 8 cm, respectively. To study the effect of the central optical hole on the accuracy of the reconstructed optical properties, we compared the reconstruction results with an extra center source and without the center source. The configuration without the center source corresponds to a 2 cm × 2 cm hole area. We further moved the noncenter 12 sources and 8 detectors toward periphery by leaving a 3 cm × 3 cm hole area in the middle. Figure 2 shows the picture of a combined probe with the 3 cm × 3 cm central area occupied by an ultrasound array. The ultrasound array consists of 64 elements made of 1.5-mm-diameter piezoelectric transducers (Valpey Fisher Inc). The

Fig. 1. Schematic arrangement of NIR source and detector fibers on the probe. Small solid circles are the source fibers and larger solid cycles are the detector fibers.

transducers are deployed in a rectangular matrix with 4-mm spacing in both $x$ and $y$ directions. The center frequency of the transducer is 6 MHz and the bandwidth is 40%. The transducers are made from the same piece of piezoelectric transducer material. Therefore the gain difference among different transducers is less than 3 dB. The 12 dual-wavelength optical laser diode sources (760 and 830 nm) and 8 photomultiplier tube (PMT) detectors are coupled to the probe through optical fibers, which are deployed at the periphery of the two-dimensional (2-D) ultrasound array. This hybrid array deployment compromises ultrasound coherent imaging and NIR diffusive light imaging characteristics.

The 9 cm × 9 cm × 4 cm image volume underneath the probe is discretized into voxels of size 0.4 cm × 0.4 cm × 1 cm. There is a trade-off between the accurate estimation of the weight matrix $W$ and the voxel



Fig. 2. Picture of an experimental probe. An ultrasound array of 8 × 8 = 64 transducers occupies the central 3 cm × 3 cm area, and 12 dual-wavelength source fibers and 8 detector fibers are deployed at the periphery.



Fig. 3. Schematic of the NIR frequency-domain imaging system. The modulation frequency is 140 MHz. The 12 dual-wavelength source channels are switched on sequentially by a PC, and 8 detector channels receive signals in parallel. BPF, bandpass filter; OSC, oscillator.

size. Because $W_{ij}$ is a discrete approximation of the integral

$$\int_{v} G(\mathbf{r}_v, \mathbf{r}_d, \omega) U_{inc}(\mathbf{r}_v, \mathbf{r}_s, \omega) \frac{v}{D} \, d\mathbf{r}_v^3,$$

it is more accurate when the voxel size is smaller. However, the total number of reconstructed unknowns will increase dramatically with the decreasing voxel size. Furthermore, the rank of $W$ does not increase in the same order as the total number of voxels when the voxel size decreases. This suggests that neighboring $W_{ij}$'s are correlated when the voxel size is smaller, and a further decrease in voxel size will not add more independent information to the weight matrix. We found that a 0.4 cm × 0.4 cm × 1 cm voxel size is a good compromise. Therefore we used this voxel size in image reconstructions reported in this paper.

## B. Experimental Systems

### 1. Near-Infrared Imaging System

We constructed a NIR frequency-domain imaging system. The block diagram of the system is shown in Fig. 3. This system has 12 dual-wavelength source channels and 8 parallel receiving channels. On the transmission part, 12 pairs of dual-wavelength (780 and 830 nm) laser diodes are used as light sources, and their outputs are amplitude modulated at 140.000 MHz. Each one of the 12 optical combiners (OZ Optics Inc.) looks like a Y adapter, guiding the emission of two diodes of different wave-

lengths through the same thin optical fiber (approximately 0.2 mm in diameter). To reduce noise and interference, an individual driving circuit is built for each diode. As a laser diode works in series, a control board that interprets instructions from a PC is used to coordinate operations of associated components. When a single transmission channel is selected, it turns on the corresponding driving circuit so that a dc driving current can be set up for the diode. At the same time, a selected signal is sent to a rf switching unit, which distributes a rf signal to the right channel to modulate the optical output. On the reception part, eight PMTs are employed to detect diffusely reflected light from turbid media. Each PMT is housed in a sealed aluminum box, shielding both environment lights and electromagnetic fields, and an optical fiber (3 mm in diameter) couples NIR light from the detection point to the reception window of the PMT. The electrical signal converted from the optical input is generally weak and rather high in frequency, so high-gain amplification and frequency transform are necessary before it can be sampled by an analog-to-digital (A/D) board inside the PC. We built eight parallel heterodyne amplification channels to measure the response of all detectors simultaneously, which reduces the data-acquisition time. Each amplification channel consists of a rf amplifier (40 dB), a mixer in which the rf signal (OSC1, 140.000 MHz) is mixed with a local oscillator (OSC2, 140.020 MHz), a bandpass filter centered at 20 kHz, and a low-frequency amplifier of 30 dB. The heterodyned two-stage amplification scheme helps suppress wideband noises efficiently. We also generated a reference signal of 20 kHz by directly mixing OSC1 and OSC2, which is necessary for retrieving phase shifts. Eight detection signals and one reference are sampled, converted, and acquired into the PC simultaneously, in which the Hilbert transform is used to compute the amplitude and phase of each channel. The entire data acquisition takes less than 1 min, which is fast enough to acquire data from patients.

One of the challenges encountered in the design of a NIR imaging system is the huge dynamic range of signals received at various source–detector distances. For example, for a semi-infinite phantom made of 0.5% Intralipid solution, the amplitude measured at 1 cm away from a source is approximately 5000 times larger than that at 8-cm separation. In addition, the perturbation that is due to an embedded heterogeneity with optical properties similar to a tumor is normally a few percent of the background signal. As a result, a reflection-mode NIR imaging system should have at least a 120-dB dynamic range to probe a target up to 4 cm in depth. It is hard to build amplifiers that work linearly over such a wide dynamic range. We overcome this difficulty by implementing two-level source outputs. The dc output of a laser diode is controlled when its feedback loop is adjusted, whereas the rf signal is switched simultaneously by a two-step attenuator (no attenuation or 30-dB attenuation). When the source and detector are close to each other, the source is controlled to

yield a low-level output. When the separation becomes larger, a 30-dB higher output level should be used. With this two-level source scheme, our system achieved fairly good linearity over a wide range of source–detector separations (from 1.5 to 8 cm).

Because the parameters of an individual laser diode or a PMT vary considerably from one to another, we have to calibrate the gain and phase shift for each channel. A set of measurements obtained from all source–detector pairs placed on the boundary of a homogeneous medium is

$$\bar{A}_{\alpha\beta}, \quad \bar{\phi}_{\alpha\beta}, \qquad \alpha = 1, 2, \ldots, m; \qquad \beta = 1, 2, \ldots, n.$$

Here, amplitude $\bar{A}_{\alpha\beta}$ and phase $\bar{\phi}_{\alpha\beta}$ are related to source $\alpha$ and detector $\beta$, and $m$ and $n$ are the total number of sources and detectors, respectively. From the diffusion theory, we can obtain the following set of equations[7]:

$$\bar{A}_{\alpha\beta} = I_s(\alpha)I_d(\beta) \frac{\exp(-k_i\rho_{\alpha\beta})}{\rho_{\alpha\beta}^2},$$

$$\bar{\phi}_{\alpha\beta} = \varphi_s(\alpha) + \varphi_d(\beta) + k_r\rho_{\alpha\beta},$$

in which $I_s(\alpha)$ and $\varphi_s(\alpha)$ are the relative gain and phase delay associated with source channel $\alpha$, $I_d(\beta)$ and $\varphi_d(\beta)$ are similar quantities associated with detector channel $\beta$, $\rho_{\alpha\beta}$ is the corresponding separation, and $k_r + jk_i$ is the complex wave number. We obtain the following set of linear equations by taking a logarithm of the above equations related to amplitude:

$$\log(\rho_{\alpha\beta}^2\bar{A}_{\alpha\beta}) = \log[I_s(\alpha)] + \log[I_d(\beta)] - k_i\rho_{\alpha\beta},$$

$$\bar{\phi}_{\alpha\beta} = \varphi_s(\alpha) + \varphi_d(\beta) + k_r\rho_{\alpha\beta}. \tag{3}$$

Although the optical properties of the calibration medium are known in advance, we leave the wave number as a variable and use fitted $k_r$ and $k_i$ to calculate the background scattering and absorption coefficients. We verified our calibration method by comparing the best fitted $k$'s with real values. The results of our using 0.5–0.8% Intralipid solutions always yielded scattering and absorption coefficients with a rather good accuracy. With the two unknown wave numbers included, the total number of unknowns is $2(m + n + 2)$, which is generally far smaller than the number of measurements $m \times n$. Consequently, Eq. (3) is overdetermined. We can solve all $I_s(\alpha)$, $I_d(\beta)$, $\varphi_s(\alpha)$, and $\varphi_d(\beta)$ terms as well as two unknown wave numbers in a least-squares sense. Then all measurements can be calibrated accordingly. The results of amplitude $A_{\alpha\beta} = \exp(-k_i\rho_{\alpha\beta})/\rho_{\alpha\beta}^2$ and phase $\phi_{\alpha\beta} = k_r\rho_{\alpha\beta}$ after calibration are shown in Fig. 4. As one can see, the calibrated amplitude ($\log \rho_{\alpha\beta}^2A_{\alpha\beta}$) and the phase from various source–detector pairs change linearly with distance.

### 2. Ultrasound System

The ultrasound system diagram is shown in Fig. 5, and the system consists of 64 parallel transmission and receiving channels. Each transmission circuit can generate a high-voltage pulse of 200-ns duration (6 MHz) with 125 V peak to peak to the connected

(a)



(b)
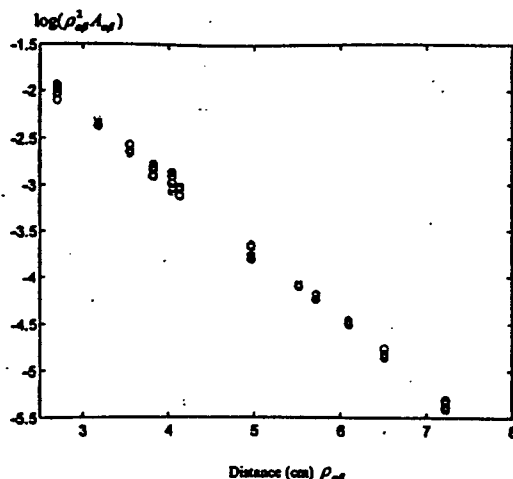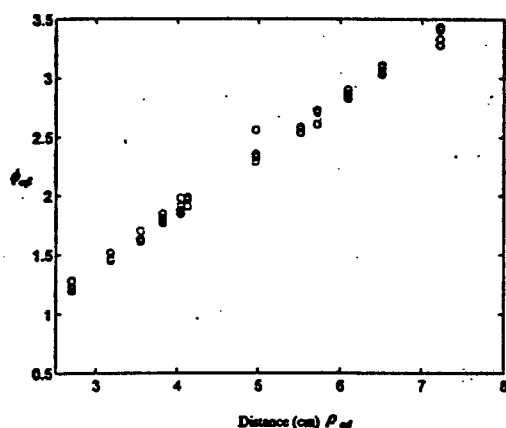
**Fig. 4.** (a) Log($\rho_{\alpha\beta}^2 A_{\alpha\beta}$) versus distance $\rho_{\alpha\beta}$ after calibration. (b) Phase $\phi_{\alpha\beta}$ versus distance $\rho_{\alpha\beta}$ after calibration.

transducer. Each receiving circuit has two-stage amplifiers followed by an A/D converter with 40-MHz sampling frequency. The amplifier gain can be controlled based on the target strength. A group of transmission channels can be addressed simultaneously to transmit pulses from neighbor transducers with specified delays and therefore to focus the transmission beam. The retuned signals can be received simultaneously by a group of transducers, and the signals can be summed with specified delays to form a receiving beam.

The data-acquisition procedure is the following. The first 9-element neighbor subarray (dashed rectangle in Fig. 6) from the 64-element transducer array and the corresponding channels are chosen, and then the transmission delay profiles are generated in the computer according to the prespecified focal depth. The delay profile data are transferred to the 64-channel delay profile generator, which triggers the 64 high-voltage pulsers as well as the receiving channels. The returned ultrasound signals are amplified
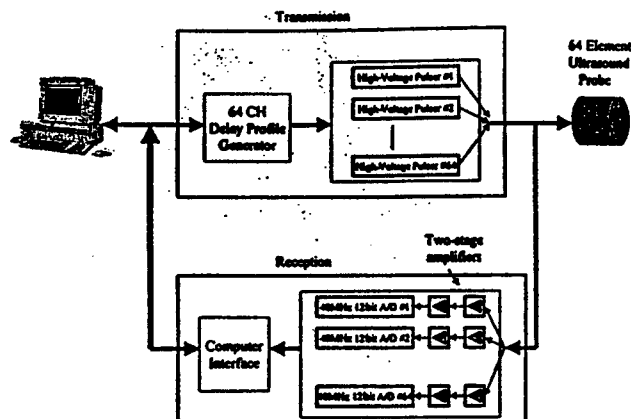


**Fig. 5.** Schematic of our ultrasound scanner. We connected 64 ultrasound transducers to 64 parallel transmission and reception channels. The transmission part consists of 64 high-voltage pulsers, which can be controlled by computer-generated delay profiles. The reception part consists of 64 two-stage amplifiers and A/D converters. CH, channel.

by two-stage amplifiers and sampled by A/D converters. The data are buffered in the memories and are read by the computer after the entire data acquisition is completed. The second subarray (solid rectangle in Fig. 6) is chosen and the same data-acquisition process is repeated. A total of 64 subarrays is used in the data acquisition. After the 64-subarray data acquisition is completed, the data stored in the memories are read by the computer for image formation. The entire data acquisition and imaging display are performed in approximately 5 s, which is fast enough for clinical experiments. To ensure good signal-to-noise ratio, we perform all the electronics using printed circuit boards.

Figure 7 shows the picture of the entire system and the combined probe. Both the NIR system (top) and the ultrasound system (bottom) are mounted on a hospital cart. The combined probe, which houses the ultrasound array and the NIR source–detector fibers, is designed to be hand held to scan patients.
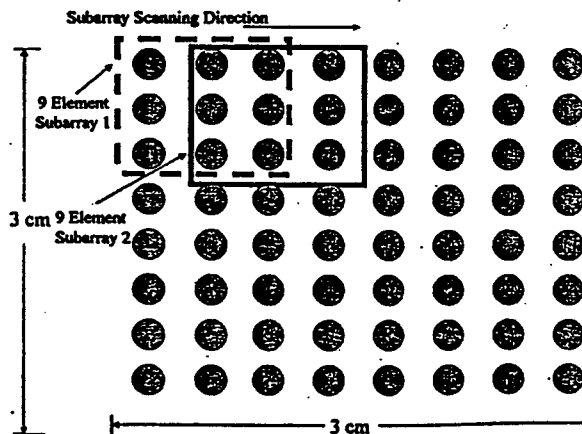


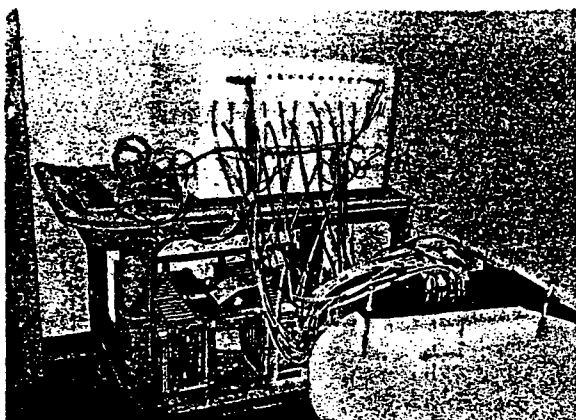**Fig. 6.** Ultrasound subarray scanning configuration.

Fig. 7. Picture of our combined system. NIR system (top) and ultrasound system (bottom) are mounted on a hospital cart.

## C. Phantoms

We used 0.5–0.6% Intralipid solutions to mimic normal human breast tissues in all experiments, and the corresponding reduced scattering coefficient $\mu_s'$ ranges from 5 to 6 cm$^{-1}$. The Intralipid is contained in a large fish tank to set up approximately a semi-infinite homogeneous phantom. Small semispherical balls (1 cm in diameter), made of acrylamide gel,[22] are inserted into Intralipid to emulate lesions embedded in a breast. The reduced scattering coefficients of the gel phantoms are similar to that of the background medium ($\mu_s' \sim 6$ cm$^{-1}$), and we changed the absorption coefficients to different values by adding different concentrations of India ink to emulate high-contrast ($\mu_a = 0.25$-cm$^{-1}$) and low-contrast ($\mu_a = 0.1$-cm$^{-1}$) lesions. Ultrasound scattering particles of 200 μm in diameter are added to the gel phantom before the gel is formed.

## 4. Experimental Results

### A. Effects of Missing Optical Sources in the Combined Probe

A series of experiments was conducted to estimate the optimal hole size. Three probe configurations were investigated: (a) no-hole, (b) 2 cm × 2 cm central hole, and (c) 3 cm × 3 cm hole probes. The no-hole probe was essentially the same as case (b) except that an additional light source was added in the middle. Figure 8 shows reconstructed NIR images for on-center targets of high ($\mu_a = 0.25$ cm$^{-1}$, left column) and low contrast ($\mu_a = 0.1$ cm$^{-1}$, right column) located 2.5 cm deep inside the Intralipid. The fitted background $\mu_a$ and $\mu_s$ are 0.015 and 5.36 cm$^{-1}$, respectively. With the target depth provided by ultrasound, we performed reconstruction in the target layer. The centers of the voxels in this layer were ($x$, $y$, 2.5 cm), where $x$ and $y$ were discrete spatial x–y coordinates, and the thickness of the layer was 1 cm. For the high-contrast target case, there are no important differences in image quality associated with different probes [Figs. 8(a) and 8(c)] except that with a 3 cm × 3 cm hole. The first row of Table 1 provides

measured maximum $\mu_a$ values from the corresponding images. Because of the low spatial resolution of diffusive imaging, the boundaries of the targets are not well defined. The maximum value is a better estimation of reconstructed target $\mu_a$. From no hole to 2 cm × 2 cm, the reconstructed maximum $\mu_a$ decreases slowly. But for 3 cm × 3 cm, the maximum $\mu_a$ drops suddenly to 0.104 cm$^{-1}$, which is less than half of the original value. Another imaging parameter we measured is the full width at half-maximum (FWHM) of the corresponding images. Because the image lobes were elliptical in general, we measured the widths of longer and shorter axes and used the geometric mean to estimate the FWHM. The results are shown in Table 1, and the FWHM almost increases with the hole size. We also measured the image artifact level, which was defined as the ratio of the peak artifact to the maximum strength of the image lobe and is given in decibels. The results are shown in Table 1. No artifacts were observed in the images of no-hole and 2 cm × 2 cm hole probes. However, the peak artifact level at the −14.3-dB level was measured in the image of the 3 cm × 3 cm hole probe. When the contrast was low, the reconstructed maximum absorption coefficients and measured FWHMs were essentially the same for the no-hole and 2 cm × 2 cm hole probes. However, the reconstructed maximum value dropped to 60% of the true value for the 3 cm × 3 cm probe. The artifact levels measured in the images of three probe configurations were similar and were worse than the high-contrast case. The image artifacts are related to the reconstruction algorithm. When the target contrast is weak or the signal-to-noise ratio is low, the inversion algorithm produces artifacts around the edges of the images.

For shallow targets (here we set the target depth to be 1.5 cm) the NIR system has a relatively poorer performance. This is due to less source–detector pairs experiencing the existence of a shallow absorber. As shown in Fig. 9, image artifacts are obviously worse compared with Fig. 8. However, the conclusion about the hole size of the probe remains true. Table 2 lists all the measured imaging parameters obtained from three probe configurations. Although a 3 cm × 3 cm hole is somewhat too big to obtain good enough results, the optimal hole size is in the neighborhood of 2 cm × 2 cm. This optimal size is approximately the size of commercial ultrasound transducers.

In the above studies, we used the iteration number obtained from the no-hole configuration for the rest of the configurations. Ideally, the iteration should stop when the object function [see Eq. (2)] or the error performance surface reaches the noise floor. However, system noise, particularly coherent noise, was difficult to estimate from experimental data. In general, we found that the reconstructed values were closer to true values when the object function reached approximately 5–15% of the initial value (total energy in the measurements). Therefore we used this criterion (~10% of the initial value) for the no-hole configuration. Because the signal-to-noise ratio of

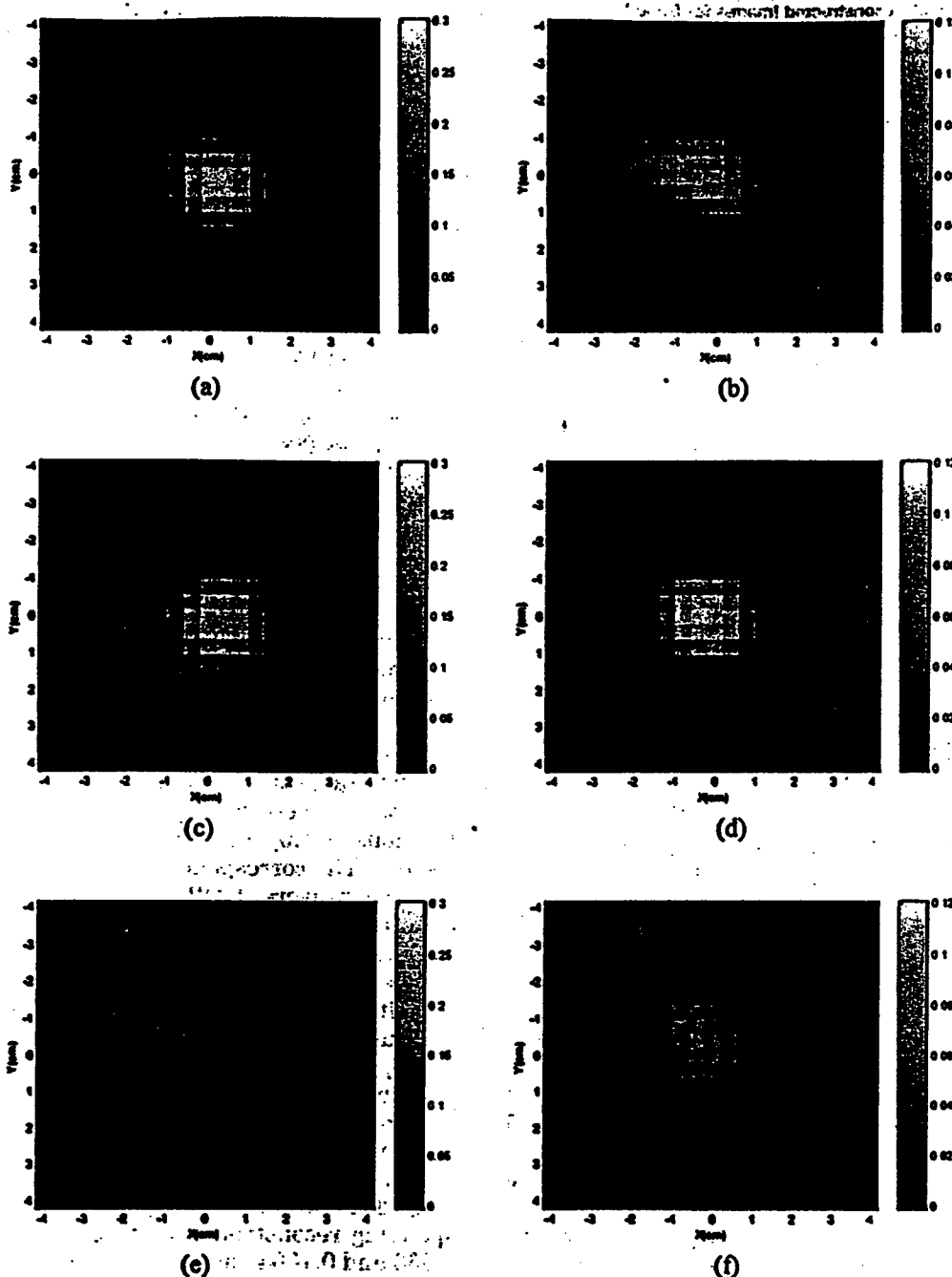**Fig. 8.** Reconstructed NIR images of deeper targets (2.5 cm in depth, 1 cm in diameter, and the fitted background $\mu_a$ and $\mu_s'$ are 0.015 and 5.36 cm$^{-1}$, respectively). The left column corresponds to images of a high-contrast target ($\mu_a$ = 0.25 cm$^{-1}$) obtained from different probe configurations, and the right column corresponds to images of a low-contrast target ($\mu_a$ = 0.1 cm$^{-1}$). Each row is related to a specific hole size: (a) and (b) no hole, (c) and (d) 2 cm $\times$ 2 cm, (e) and (f) 3 cm $\times$ 3 cm.

the data decreased with the increase in hole size, we could not find consistent criterion for both no-hole and hole data. Therefore we used the same iteration number obtained from the no-hole case for the hole configurations, and the comparison was based on the same iteration number.

**B. Ultrasound-Guided Near-Infrared Imaging**

Three-dimensional ultrasound images can provide 3-D distributions of targets. With the *a priori* target

depth information, the optical reconstruction can be improved significantly. An example is given in Fig. 10. The target again was a 1-cm-diameter gel ball of low ($\mu_a$ = 0.1-cm$^{-1}$) optical contrast and was embedded at approximately (0, 0, 2.5 cm) inside the Intralipid medium. The fitted background $\mu_a$ and $\mu_s'$ are 0.02 and 5.08 cm$^{-1}$, respectively. The combined probe shown in Fig. 2 was used to obtain the ultrasound and NIR data simultaneously. Figure 10(a) shows an A-scan line of a returned ultrasound echo

**Table 1. Parameters of Reconstructed Images for Deep High-Contrast ($\mu_a = 0.25$-cm$^{-1}$) and Low-Contrast ($\mu_a = 0.1$-cm$^{-1}$) Targets[a]**

| | Probe Type | | |
|---|---|---|---|
| Parameter | No Hole | 2 cm × 2 cm | 3 cm × 3 cm |
| **High contrast** | | | |
| $\mu_{a(max)}$[b] (cm$^{-1}$) | 0.251 | 0.234 | 0.104 |
| FWHM[c] (cm) | 1.85 | 1.91 | 2.44 |
| Artifacts (dB) | Background (−22) | Background | −14.3 |
| **Low contrast** | | | |
| $\mu_{a(max)}$ (cm$^{-1}$) | 0.105 | 0.111 | 0.064 |
| FWHM (cm) | 2.02 | 1.83 | 2.16 |
| Artifacts (dB) | −6.90 | −8.10 | −5.65 |

[a]The fitted background $\mu_a$ and $\mu_s'$ are 0.015 and 5.36 cm$^{-1}$, respectively.

[b]$\mu_{a(max)}$ is the measured maximum value of the reconstructed absorption coefficient map.

[c]FWHM is defined as the geometric mean of the widths measured at longer and shorter axes of the elliptical image lobe.

signal received by one ultrasound transducer located on top of the target. As acoustic scatters were uniformly distributed in the target, signals were reflected from inside the target as well as from the surfaces. The reflected signals from the front and back surfaces of the gel ball can be clearly identified in the echo signal. On the basis of the target depth, we reconstructed the optical absorption coefficient at the target depth only (1 cm in thickness) by setting the perturbations from the other depths equal to zero. We also performed 3-D optical-only reconstruction. Figure 10(b) shows the reconstructed absorption image from a 3-D optical-only reconstruction [layer three of voxel coordinates ($x, y$, 2.5 cm) and 1 cm thick], whereas Fig. 10(c) shows the reconstructed image of the corresponding target from ultrasound-guided reconstruction. For optical-only reconstruction, the algorithm did not converge to a localized spatial region, and the image contrast was poor. The measured maximum absorption coefficient was 0.088 cm$^{-1}$, which was close to the true value. However, the measured spatial location of the maximum value was (−1.6, −1.2 cm), which was too far from the true target location. With the *a priori* target depth, the reconstruction performed at the target layer can localize the target to the correct spatial position. The measured maximum absorption coefficient was 0.12 cm$^{-1}$ and its location was (0, 0.4 cm), which was very close to the true target location. This example demonstrates that *a priori* target depth can significantly improve the reconstruction accuracy and target localization.

In addition to use of *a priori* target depth information, we can also use the target spatial distribution provided by ultrasound to guide the reconstruction. We performed a set of experiments with two targets

located at 2.5 cm in depth inside the Intralipid. Each target is a 1-cm$^3$ gel cube containing ultrasound scatters. For optical properties, they both could be high contrast ($\mu_a = 0.25$ cm$^{-1}$) or low contrast ($\mu_a = 0.1$ cm$^{-1}$), but had the same reduced scattering coefficient as the background. The fitted background $\mu_a$ and $\mu_s'$ are 0.017 and 4.90 cm$^{-1}$, respectively. One target was centered approximately at (−1.0, −1.0, 2.5 cm), whereas the other was at (1.0, 1.0, 2.5 cm). The distance between the centers of the two targets was 2.8 cm.

Figure 11(a) is the ultrasound image of two high-contrast targets. As the field of view of the ultrasound system was nearly a 3 cm × 3 cm square, these two targets appeared at diagonal corners. The measured peak positions of the two targets were (−0.6, −1.0 cm) and (1.0, 1.0 cm), which differed from the true target locations by only one voxel. The low contrast of the ultrasound image is related to the speckle noise. Because our ultrasound array is sparse, the imaging quality is not state of the art (see more discussion in Section 5). The NIR image of these targets was obtained simultaneously and is shown in Figure 11(b). We performed the reconstruction at the target layer by taking advantage of target depth information. A total of 123 iterations was used to obtain Fig. 11(b). The measured peak positions of the two targets were (−1.4, −1.0 cm) and (0.6, 0.6 cm), which were one voxel off from the true target locations (−1.0, −1.0 cm) and (1.0, 1.0 cm), respectively. The corresponding reconstructed absorption coefficients were 0.242 and 0.251 cm$^{-1}$, which were close to the true values. However, the two targets were almost connected to each other, and their spatial localization was poor. For low-contrast targets, the ultrasound image is shown in Fig. 11(c), and the measured peak locations of the two targets were (−1.0, −0.6 cm) and (0.6, 1.0 cm), which differed from the true target locations by only one voxel. The corresponding NIR image is shown in Fig. 11(d), and the measured peak locations of the two targets were (−2.2, −1.0 cm) and (0.6, 1.0 cm). The left target was off the true location by three voxels. The corresponding reconstructed absorption coefficients were 0.063 and 0.1004 cm$^{-1}$ at 87 iteration steps. As one can see, the target shape and localization were poorer than those in the high-contrast case. In addition, an artifact appeared at the edge of the image.

From the coregistered ultrasound images, we obtained spatial distributions of the two targets and specified target regions. Figures 12(a) and 12(c) show the −6-dB contour plots of Figs. 11(a) and 11(c). Applying the same reconstruction scheme to these specific regions, we obtained Figs. 12(b) and 12(c) in one iteration. The reconstructed absorption coefficients were 0.2357 and 0.219 cm$^{-1}$ for the two high-contrast target cases and 0.123 and 0.131 cm$^{-1}$ for the low-contrast case. We can see much better improvement in the low-contrast target case when we compare Fig. 12(d) with Fig. 11(d). This example demonstrates that, when the targets are visible in ultrasound images, their morphology information
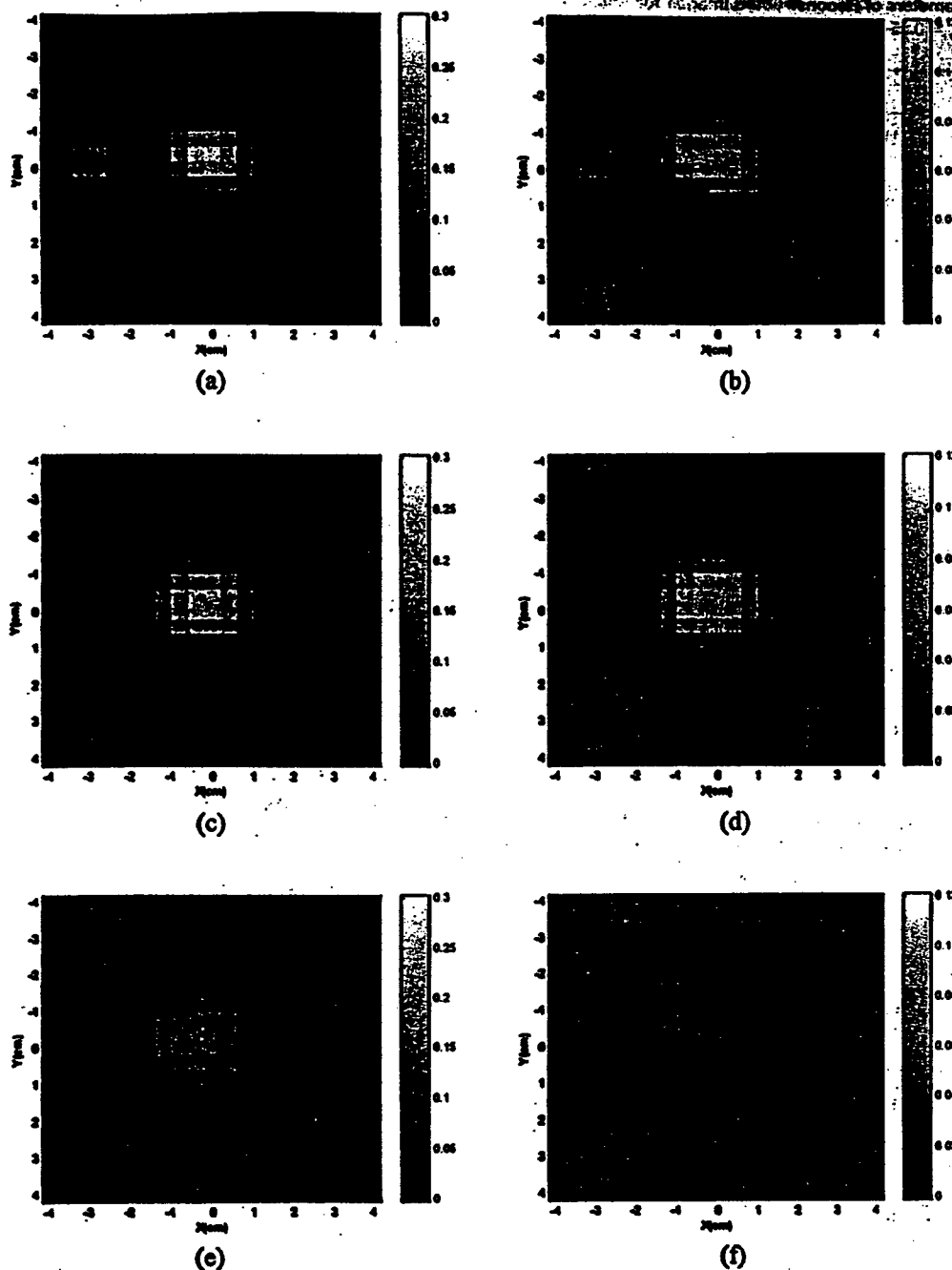
Fig. 9. Reconstructed NIR images for shallow targets (1.5 cm in depth, 1 cm in diameter, and the fitted background $\mu_a$ and $\mu_s'$ are 0.015 and 5.36 cm$^{-1}$, respectively). The left column corresponds to images of a high-contrast target ($\mu_a$ = 0.25 cm$^{-1}$), and the right column corresponds to images of a low-contrast target ($\mu_a$ = 0.1 cm$^{-1}$). Each row is related to a specific hole size: (a) and (b) no hole, (c) and (d) 2 cm $\times$ 2 cm, (e) and (f) 3 cm $\times$ 3 cm.

provided by ultrasound can be used to guide the optical reconstruction in the specified regions.

The result regarding the iteration step is significant. As we discussed above, there is no known stopping criterion to terminate the iteration because it is difficult to estimate the noise level in the measurements. With the *a priori* target depth and spatial distribution provided by coregistered ultrasound, we can obtain an accurate optical absorption coefficient in one iteration. Therefore no stopping crite-

rion is needed for the inversion algorithms. However, this result will need to be further evaluated with more samples of different contrasts.

## 5. Discussion

Commercial ultrasound scanners use one-dimensional probes that provide 2-D images of x–z views of the targets, where x and z are the spatial and propagation dimensions, respectively. Such x–z images cannot coregister with NIR images, which are

**Table 2. Parameters of Reconstructed Images for Shallow High-Contrast ($\mu_a = 0.25\text{-cm}^{-1}$) and Low-Contrast ($\mu_a = 0.1\text{-cm}^{-1}$) Targets[a]**

| | Probe Type | | |
|---|---|---|---|
| Parameter | No Hole | 2 cm × 2 cm | 3 cm × 3 cm |
| **High contrast** | | | |
| $\hat{\mu}_{a(max)}$ ($\text{cm}^{-1}$) | 0.250 | 0.194 | 0.118 |
| FWHM (cm) | 1.32 | 1.61 | 2.08 |
| Artifacts (dB) | −7.98 | −12.7 | −9.76 |
| **Low contrast** | | | |
| $\hat{\mu}_{a(max)}$ ($\text{cm}^{-1}$) | 0.100 | 0.091 | 0.042 |
| FWHM (cm) | 1.88 | 2.11 | 3.17 |
| Artifacts (dB) | −6.25 | −7.44 | −0.65 |

[a]The fitted background $\mu_a$ and $\mu_s'$ are 0.015 and 5.35 $\text{cm}^{-1}$, respectively.

obtained from $x$–$y$ views of the targets. Our current 2-D ultrasound array is capable of providing $x$–$y$ views of the targets, which can be used to coregister with NIR images. However, the array is sparse and therefore the image resolution is not state of the art. Nevertheless, its spatial resolution is comparable to NIR imaging and can be used to guide NIR image reconstruction. With 3-D ultrasound guidance, only one iteration is needed to obtain accurate absorption coefficients. This result is significant because no stopping criterion is necessary. More studies with a variety of target contrasts and locations will be performed to verify this result.

We purchased a 2-D state-of-the-art ultrasound array of 1280 transducer elements and we are building a multiplexing unit for our 64-channel electronics. In addition, the new 2-D transducer size is approximately 2 cm × 3 cm, which is in the neighborhood of the optimal hole size we found through this study. With the new 2-D ultrasound transducer, we will be able to obtain high-resolution ultrasound images and delineate the target boundaries with finer details for optical reconstruction.

Ultrasound contrast depends on lesion acoustic properties, and NIR optical contrast is related to lesion optical properties. Both contrasts exist in tumors, but the sensitivities of these two modalities may be different. It is possible that some early-stage cancers have NIR contrast but are not detectable by ultrasound. It would be desirable if we could obtain sensitivity of optical imaging alone. However, light scattering is a main problem that prevents the accurate and reliable localization of lesions. It is also possible that some lesions have acoustic contrast but no NIR contrast or low NIR contrast. Currently, ultrasound is routinely used as an adjunct tool to x-ray mammography; the combined sensitivity of these two modalities in breast cancer detection is

more than 90%.[29] Recently, ultrasound has also been advocated to screen dense breasts.[30] We anticipate that our combined imaging will add more specificity to the ultrasonically detected lesions.

In the reported phantom studies, we assigned zero perturbations to the regions where no targets were present. In clinical studies, we plan to segment the ultrasound images and specify different tissue types as well as suspicious regions in the segmented images. We will then reduce the reconstructed optical unknowns by assigning unknown optical properties to different tissue types as well as to suspicious regions. Finally, we will reconstruct the reduced sets of unknown optical properties. We expect a more accurate estimation of reconstructed optical properties and fast convergence speed, as reported in this paper. However, it is still too early to judge the clinical performance of the combined method; further clinical studies are needed.

Probing regions of the banana-shaped diffusive photons depend on source–detector separations and measurement geometry. For a semi-infinite geometry, the probing regions extend further into the medium when source–detector separation increases. This is why we have multiple source–detector pairs of various separations to detect targets at variable depths from 0.5 to 4 cm. Of course it is hard to achieve uniform sensitivity in the entire region of interest. For example, a superficial target ($\sim$1 cm deep) would cause strong perturbations when it is close to a source or a detector, but will result in much weaker signals when it is located deeper. Normalization of scattering photon density waves with respect to the incident waves makes it possible for reconstruction algorithms to handle the huge dynamic range of signals and to detect a target as deep as 4 cm. This normalization procedure was applied to the reconstruction algorithm used to obtain the reported images.

In this study, the target absorption coefficient was reconstructed from the measurements. Because the target $\mu_s'$ was similar to the background $\mu_s'$, the coupling between $\mu_a$ and $\mu_s'$ in our measurements was negligible. We also performed experiments with gel phantom made with Intralipid with a concentration similar to that of the background and did not observe perturbation beyond the noise level. Similar reconstruction studies can be performed for scattering coefficients as well. Simultaneous reconstruction of both absorption and scattering coefficients is also possible. Because the eigenvalues of the absorption and scattering weight matrices are significantly different, good regulation schemes are needed for simultaneous reconstruction. This subject is one of our topics for further study.
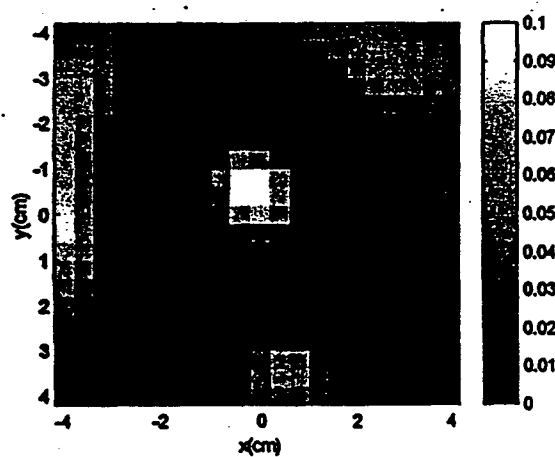
## 6. Summary

We have constructed a near-real-time imager that can provide coregistered ultrasound and NIR images simultaneously. This new technique is designed to improve the specificity of breast cancer diagnosis. Because the ultrasound transducer needs to occupy
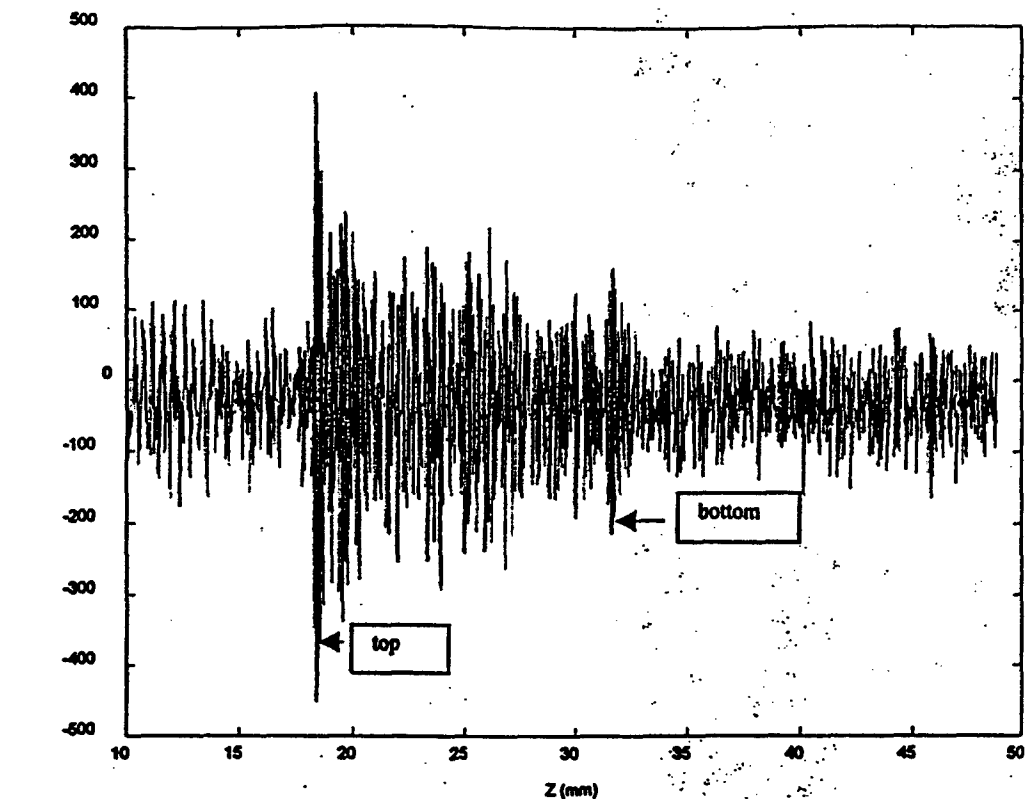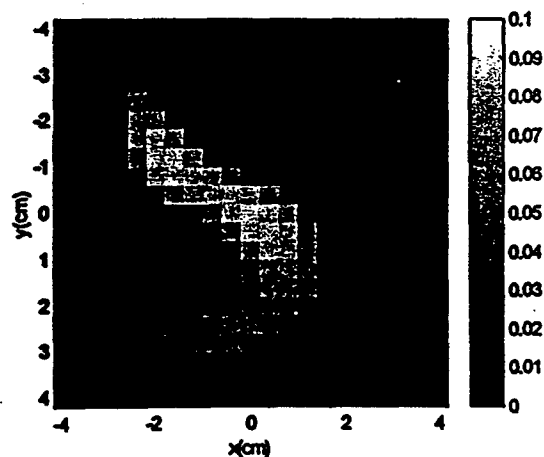
Fig. 10. Deep target (2.5 cm in depth, 1 cm in diameter) of low optical contrast ($\mu_a = 0.10$ cm$^{-1}$ and fitted background $\mu_a$ and $\mu_s'$ are 0.02 and 5.08 cm$^{-1}$, respectively). (a) A-scan line of the reflected ultrasound pulse-echo signal indicating the target depth. (b) Absorption image of the low-contrast target obtained from optical-only reconstruction. (c) Ultrasound-guided reconstruction at target depth.

the central region of the combined probe, a series of experiments were conducted to investigate the effects of missing optical sensors in the middle of the combined probe on the NIR image quality. Our results have shown that, as long as the central ultrasound transducer area is in the neighborhood of 2 cm × 2 cm, essentially similar reconstruction results as those of no missing optical sensors in the middle of the combined probe can be obtained. This 2 cm × 2 cm dimension is approximately the size of most commercial ultrasound phased-array transducers. When the central missing optical sensor area is in-
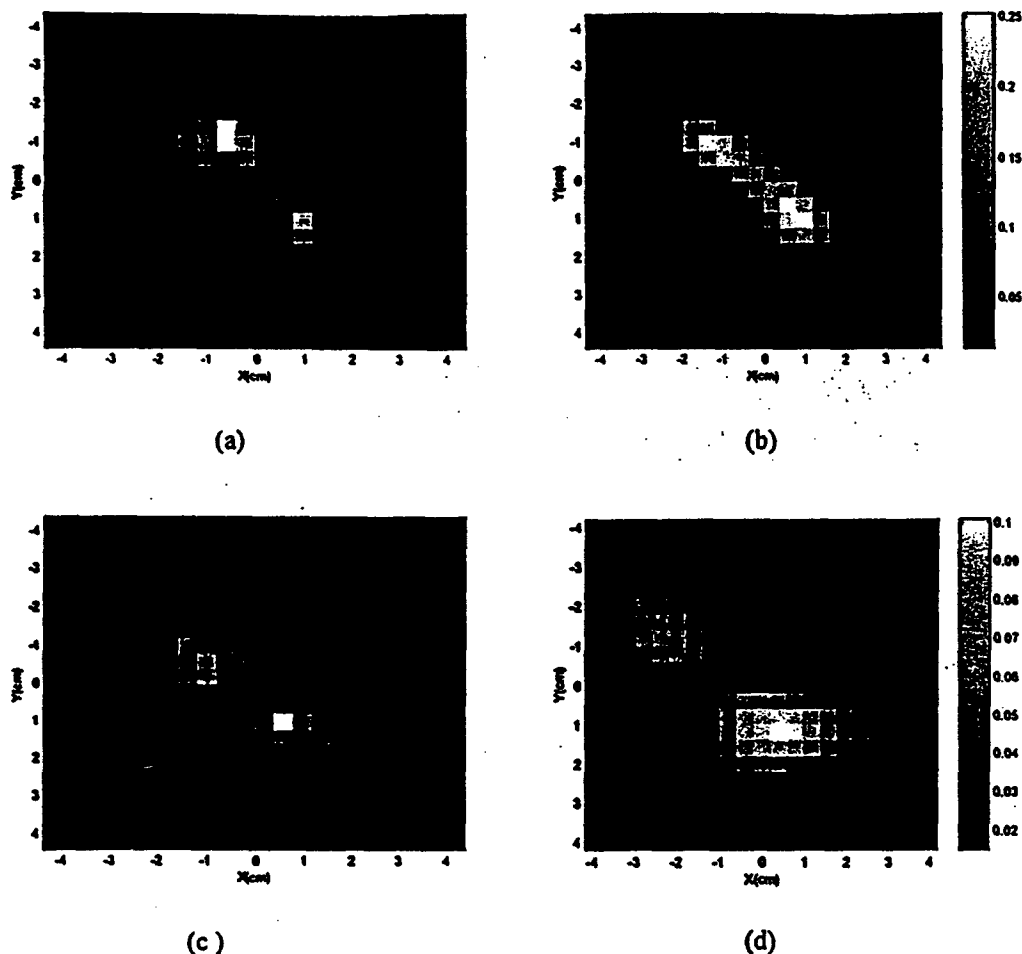
Fig. 11. Simultaneously obtained ultrasound and NIR absorption images. The fitted background $\mu_a$ and $\mu_s'$ are 0.017 and 4.90 cm$^{-1}$, respectively. (a) Ultrasound and (b) NIR absorption image of two high-contrast targets (target $\mu_a = 0.25$ cm$^{-1}$). (c) Ultrasound and (d) NIR image of two low-contrast targets (target $\mu_a = 0.10$ cm$^{-1}$). In both high- and low-contrast cases, the two targets were located at 2.5 cm in depth.

creased to 3 cm × 3 cm, however, the reconstructed values are obviously lower than real values. If we increase the iteration steps, artifacts in the reconstructed images would soon become dominant.

With the target 3-D distribution provided by coregistered ultrasound, significant improvements in algorithm convergence and reconstruction speed were achieved. In general, *a priori* target depth information guides the inversion algorithm to reconstruct the heterogeneities at the correct spatial locations and improves the reconstruction speed by an order of magnitude. In addition, the *a priori* target spatial distribution can further reduce the iteration to one step and also obtain accurate optical absorption coefficients. Given the fact that no known stopping criterion is available, this result is significant because no iteration is needed. However, this result will need to be evaluated with more samples of different contrasts.

References

1. T. A. Stavros, D. Thickman, and C. Rapp, "Solid breast nodules: use of sonography to distinguish between benign and malignant lesions," Radiology 196, 123–134 (1995).
2. G. Rahbar, A. C. Sie, G. C. Hansen, J. S. Prince, M. L. Melany, H. Reynolds, V. P. Jackson, J. W. Sayre, and L. W. Bassett, "Benign versus malignant solid breast masses: US differentiation," Radiology 213, 889–894 (1999).
3. V. P. Jackson, "The current role of ultrasonography in breast imaging," Radiol. Clin. North Am. 33, 1161–1170 (1995).
4. B. Tromberg, N. Shah, R. Lanning, A. Cerussi, J. Espinoza, T. Pham, L. Svaasand, and J. Butler, "Non-invasive in vivo characterization of breast tumors using photon migration spectroscopy," Neoplasia 2, 26–40 (2000).
5. S. Fantini, S. Walker, M. Franceschini, M. Kaschke, P. Schlag, and K. Moesta, "Assessment of the size, position, and optical properties of breast tumors in vivo by noninvasive optical methods," Appl. Opt. 37, 1982–1989 (1998).
6. S. M. Nioka, M. Shnall, M. Miwa, S. Orel, M. Haida, S. Zhao, and B. Chance, "Photon imaging of human breast cancer," Adv. Exp. Med. Biol. 16, 171–179 (1994).
7. R. M. Danen, Y. Wang, X. D. Li, W. S. Thayer, and A. G. Yodh,
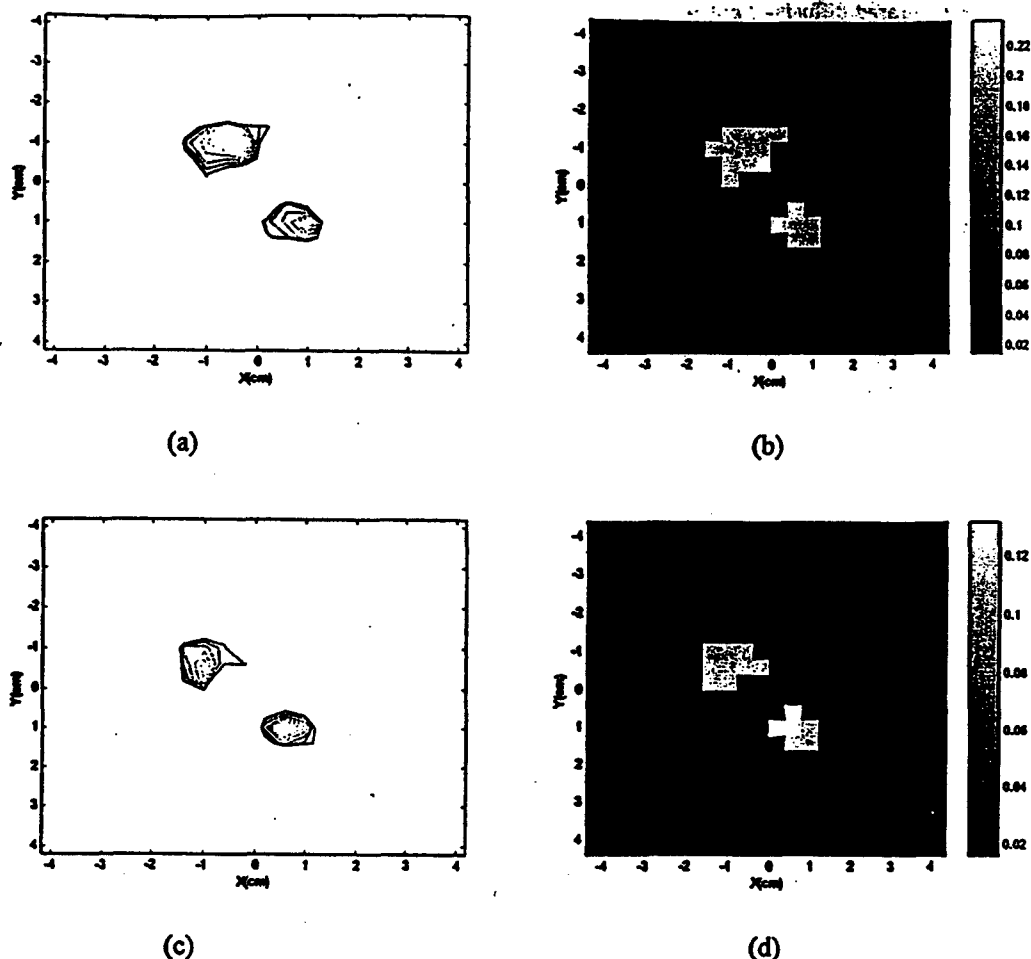
(a)   (b)   (c)   (d)

Fig. 12. (a) and (c) −6-dB contour plots of ultrasound images shown in Figs. 11(a) and 11(c). The outer contour is −6 dB from the peak, and the contour spacing is 1 dB. (b) and (d) Corresponding NIR absorption maps reconstructed in target regions specified by ultrasound.

"Regional imager for low resolution functional imaging of the brain with diffusing near-infrared light," Photochem. Photobiol. 67, 33–40 (1998).

8. T. McBride, B. W. Pogue, E. Gerety, S. Poplack, U. Osterberg, B. Pogue, and K. Paulsen, "Spectroscopic diffuse optical tomography for the quantitative assessment of hemoglobin concentration and oxygen saturation in breast tissue," Appl. Opt. 38, 5480–5490 (1999).

9. M. A. Franceschini, K. T. Moesta, S. Fantini, G. Gaida, E. Gratton, H. Jess, M. Seeber, P. M. Schlag, and M. Kashke, "Frequency-domain techniques enhance optical mammography: initial clinical results," Proc. Natl. Acad. Sci. USA 94, 6468–6473 (1997).

10. J. B. Fishkin, O. Coquoz, E. R. Anderson, M. Brenner, and B. J. Tromberg, "Frequency-domain photon migration measurements of normal and malignant tissue optical properties in a human subject," Appl. Opt. 36, 10–20 (1997).

11. T. L. Troy, D. L. Page, and E. M. Sevick-Muraca, "Optical properties of normal and diseased breast tissues: prognosis for optical mammography," J. Biomed. Opt. 1, 342–355 (1996).

12. R. J. Grable, D. P. Rohler, and S. Kla, "Optical tomography breast imaging," in Optical Tomography and Spectroscopy of Tissue: Theory, Instrumentation, Model, and Human Studies II, B. Chance and R. Alfano, eds., Proc. SPIE 2979, 197–210 (1997).

13. Y. Yao, Y. Wang, Y. Pei, W. Zhu, and R. L. Barbour, "Frequency-domain optical imaging of absorption and scatter-

ing distributions by a Born iterative method," J. Opt. Soc. Am. A 14, 325–341 (1997).

14. H. Jiang, K. Paulsen, U. Osterberg, B. Pogue, and M. Patterson, "Optical image reconstruction using frequency-domain data: simulations and experiments," J. Opt. Soc. Am. A. 12, 253–266 (1995).

15. X. Li, T. Durduran, A. Yodh, B. Chance, and D. N. Pattanayak, "Diffraction tomography for biomedical imaging with diffuse-photon density waves," Opt. Lett. 22, 573–575 (1997).

16. C. Matson and H. Liu, "Backpropagation in turbid media," J. Opt. Soc. Am. A 16, 1254–1265 (1999).

17. M. A. O'Leary, "Imaging with diffuse photon density waves," Ph.D. dissertation (University of Pennsylvania, Philadelphia, Pa., 1996).

18. K. Paulsen, P. Meaney, M. Moskowitz, and J. Sullivan, Jr., "A dual mesh scheme for finite element based reconstruction algorithms," IEEE Trans. Med. Imaging 14, 504–514 (1995).

19. S. Arridge and M. Schweiger, "Photon-measurement density functions. Part I: Analytical forms," Appl. Opt. 34, 7395–7409 (1995).

20. S. Arridge and M. Schweiger, "Photon-measurement density functions. II. Finite-element-method calculations," Appl. Opt. 34, 8026–8037 (1995).

21. Q. Zhu, T. Dunrana, M. Holboke, V. Ntziachristos, and A. Yodh, "Imager that combines near-infrared diffusive light and ultrasound," Opt. Lett. 24, 1050–1052 (1999).

22. Q. Zhu, D. Sullivan, B. Chance, and T. Dambro, "Combined

ultrasound and near infrared diffusive light imaging," IEEE Trans. Ultrason. Ferroelectr. Freq. Control 46, 665–678 (1999).

23. Q. Zhu, E. Conant, and B. Chance, "Optical imaging as an adjunct to sonograph in differentiating benign from malignant breast lesions," J. Biomed. Opt. 5(2), 229–236 (2000).

24. Q. Zhu, N. G. Chen, D. Q. Piao, P. Y. Guo, and X. H. Ding, "Design of near-infrared imaging probe with the assistance of ultrasound localization," Appl. Opt. 40, 3288–3303 (2001).

25. M. Jholboke, B. J. Tromberg, X. Li, N. Shah, J. Fishkin, D. Kidney, J. Butler, B. Chance, and A. G. Yodh, "Three-dimensional diffuse optical mammography with ultrasound localization in human subject," J. Biomed. Opt. 5(2), 237–247 (2000).

26. W. Zhu, Y. Wang, and J. Zhang, "Total least-squares reconstruction with wavelets for optical tomography," J. Opt. Soc. Am. A 15, 2639–2650 (1998).

27. P. C. Li, W. Flax, E. S. Ebbini, and M. O'Donnell, "Blocked element compensation in phased array imaging," IEEE Trans. Ultrason. Ferroelectr. Freq. Control 40(4), 283–292 (1993).

28. G. H. Golub, "Some modified matrix eigenvalue problems," SIAM (Soc. Ind. Appl. Math.) Rev. 15, 318–334 (1973).

29. H. Zonderland, E. G. Coerkamp, J. Hermans, M. J. van de Vijver, and A. E. van Voorthuisen, "Diagnosis of breast cancer: contribution of US as an adjunct to mammography," Radiology 213, 413–422 (1999).

30. T. M. Kolb, J. Lichy, and J. H. Newhouse, "Occult cancer in women with dense breast: detection with screening US-diagnostic yield and tumor characteristics," Radiology 207, 191–199 (1998).